ChemPubSoc Europe

DOI: 10.1002/cctc.201700299

CHEMCATCHEM Full Papers

Peptide-FlgA3-Based Gold Palladium Bimetallic Nanoparticles That Catalyze the Oxygen Reduction Reaction in Alkaline Solution

Dongliang Li,[a] Zhenghua Tang,*[b, c] Shaowei Chen,[b, d] Yong Tian,[a] and Xiufang Wang*[a]

Given the synergetic properties of different metal species, bimetallic nanoparticles are of immense scientific interest and technological importance in the field of catalysis. A peptide-based method represents a new avenue to fabricate bimetallic nanocatalysts with a controllable size, shape, composition, and subtle surface microstructure. However, the electrocatalytic abilities of these peptide-based bimetallic nanoparticles remain largely unexplored. Herein, we employed the peptide sequence FlgA3 to fabricate a series of AuPd alloys that were used as catalysts for the oxygen reduction reaction (ORR). Among the samples tested, $Au_{33}Pd_{67}$ exhibited the best activity, evidenced by the most positive onset potential and the largest diffusion-limited current. Notably, the ORR activity of $Au_{33}Pd_{67}$ was comparable with that of commercial Pt/C, and the long-term durability was significantly superior to that of Pt/C. A peptide-enabled approach might pave the way for the fabrication of bimetallic nanomaterials with enhanced electrocatalytic properties under mild conditions.

Introduction

Bimetallic nanoparticles (NPs) have the potential to advance catalysis and electrocatalysis but their biggest challenge arises from the difficulty to manipulate their composition and surface structure precisely.[1–3] It is well known that the catalytic activity of these bimetallic NPs is highly dependent on their size, shape, composition, and surface atomic arrangements.[4,5] Compared with their monometallic NP counterparts, bimetallic NPs often possess an enhanced catalytic activity, thanks to the synergetic effects that arise from the electronic and geometric effects of these bimetallic NPs. For instance, the introduction of Au to a Pd surface can significantly enhance the turnover frequency, as the more negative Au pulls electrons from Pd.[2,6] A similar phenomenon occurs if Pd or Pt is added to an Au nanostructure.[7,8] However, for geometric effects, the combination of two metals can lead to the generation of new catalytically active sites.[1,2,9]

As bimetallic NPs have an immense potential in the fabrication of sustainable catalysts with a high efficiency, the development of new synthetic techniques is of critical importance. A variety of methods have been developed to prepare bimetallic alloyed NPs. An important strategy is to tune the surface ligand or stabilizer, and recently, biological molecules such as bacteria,[10] enzymes,[11] DNA,[12] proteins,[13] and especially peptides[14,15] have gained increasing attention. Notably, compared to conventional approaches, the synthesis of peptide-based bimetallic NPs is an environmentally friendly process as it is normally conducted in water at room temperature.[16,17] Importantly, peptides can manipulate the physiochemical properties of these bimetallic NPs with exquisite atomic structural control. For example, Merrill et al. employed peptide R5 to demonstrate the fabrication of AuPd alloys, and an enhanced reactivity toward olefin hydrogenation was obtained.[18] Kim and co-workers documented the fabrication and catalytic response to oxygen reduction of surface-composition-controlled AuPt bimetallic NPs on carbon nanotubes.[19] Recently, Bedford and co-workers reported the fabrication of peptide-directed AuPd nanoscale surface segregation, and a surface-dependent catalytic activity toward methanol oxidation was observed.[20]

Despite this progress achieved on peptide-templated AuPd NPs, their electrocatalytic ability still remains largely unexplored. Besides the above examples, to date, few examples can be found. Recently, we reported the fabrication of

[a] D. Li, Prof. Y. Tian, Prof. X. Wang
School of Pharmacy
Guangdong Pharmaceutical University
Guangzhou, 510006 (P.R. China)
E-mail: x_f_wang@163.com

[b] Prof. Z. Tang, Prof. S. Chen
New Energy Research Institute,
School of Environment and Energy
South China University of Technology,
Guangzhou Higher Education Mega Center
Guangzhou, Guangdong 510006 (P.R. China)
E-mail: zhht@scut.edu.cn

[c] Prof. Z. Tang
Guangdong Provincial Key Lab of Atmospheric
Environment and Pollution Control, Guangdong Provincial
Engineering and Technology Research Center for Environmental
Risk Prevention and Emergency Disposal
South China University of Technology,
Guangzhou Higher Education Mega Centre
Guangzhou 510006 (P.R. China)

[d] Prof. S. Chen
Department of Chemistry and Biochemistry
University of California
1156 High Street
Santa Cruz, California 95064 (USA)

Supporting information for this article can be found under: https://doi.org/10.1002/cctc.201700299.

© 2017 Wiley-VCH Verlag GmbH & Co. KGaA, Weinheim

peptide-R5-templated Au and Pt nanomaterials with different morphologies as highly efficient catalysts for the oxygen reduction reaction (ORR).[21] In addition, a series of peptide-capped Pd NPs was fabricated to examine their ORR activity, and strong surface effects were established between the peptide sequence and the electrocatalytic activity.[22] Notably, the ORR is the pivotal step that determines the efficiency of a fuel cell,[23–27] which is considered widely as a promising green energy device thanks to its high energy conversion efficiency, ultrahigh power density, easy operation at low temperature, and almost no detrimental environmental impacts. The most widely employed catalysts for the ORR are Pt- and/or Pt-based nanomaterials,[28–31] however, the high price and limited earth abundance of Pt as well as the low stability of such catalysts hinders the widespread commercialization of fuel cells significantly. Au and Pd would be an excellent binary alloy as Pd interacts strongly with oxygen and Au does not.[32] Compared to compounds that include only Au[33,34] or Pd,[35,36] AuPd alloys have shown an enhanced electrocatalytic activity toward ORR.[1] The ORR activity of AuPd bimetallic alloys is determined largely by their structural features, which include size, morphology, composition, and surface atomic distribution, hence efforts have been devoted to the manipulation of these features. Wang and co-workers prepared AuPd-chain networks by a one-pot approach, and the as-prepared networks exhibited a superior ORR activity to commercial Pd black.[37] Deming et al. documented alkyne-protected AuPd NPs for the ORR, and the best performance was identified with a sample composed of 91.2% Pd.[32] Recently, our group demonstrated the fabrication of supported ultra-small AuPd clusters for the ORR, and a comparable activity with a markedly higher stability than commercial Pt/C was obtained.[38] These results indicate clearly that AuPd alloys have a great potential as alternative non-Pt catalysts for the ORR, however, to the best of our knowledge, a peptide-enabled approach to fabricate such alloys for the ORR is still lacking. This is the primary motivation of our present investigation.

FlgA3, which has a sequence of DYKDDDDKPAYSSGAPPMPPF, was first synthesized by Slocik and Naik.[39] It contains two domains of A3 and Flg. The A3 domain (AYSSGAPPMPPF) is able to stabilize the Au surface and form stable NPs,[40] whereas the Flg domain holds potential binding sites for metal substrates that include Pd. Slocik and Naik used the FlgA3 sequence to demonstrate the fabrication of a Au@Pd core–shell structure with a high catalytic activity in the hydrogenation of 3-buten-1-ol.[39]

In this study, FlgA3 was employed as the template and stabilizer to fabricate bimetallic AuPd NPs with enhanced electrocatalytic activity toward the ORR. Among a series of samples, $Au_{33}Pd_{67}$ exhibited the best activity, evidenced by the most positive onset potential and largest diffusion-limited current. Notably, the ORR activity of $Au_{33}Pd_{67}$ was comparable to that of commercial Pt/C, and its long-term durability was remarkably higher than that of Pt/C.

Results and Discussion

Peptide-FlgA3-based AuPd bimetallic NPs were fabricated through a modification of a procedure reported previously.[39,41] The UV/Vis absorbance spectra of the AuPd alloys are shown in Figure S1. Interestingly, no characteristic absorbance peak at approximately $\lambda = 520$ nm is observed for the alloy samples, and the absence of the surface plasmon peak indicates that relatively small particles or clusters were formed.[42,43] The samples were examined by using TEM and high-resolution transmission electron microscopy (HRTEM). A representative TEM image and corresponding size distribution histogram of the alloyed samples is shown in Figure S2. The alloyed NPs were rather well dispersed without clear aggregation, which indicates effective passivation by FlgA3. The average NP size fluctuated in the narrow range of 3–5 nm (Table 1). The slight sample-to-sample size variation is probably a consequence of the NP growth dynamics, in which ligand passivation competes with metal core nucleation.[44]

Table 1. Summary of the AuPd alloys, which include size, onset potential, diffusion-limited current, and electron transfer number (*n*) for the ORR.

Sample	FlgA3/ Au/Pd	Size [nm]	E_{onset} [nm]	Diffusion-limited current [mA cm^{-2}]	*n*
Pd_{100}	1:0:60	3.55 ± 0.97	0.89	−4.83	3.88–3.95
$Au_{20}Pd_{80}$	1:12:48	2.65 ± 0.34	0.90	−4.91	3.83–3.94
$Au_{33}Pd_{67}$	1:20:40	2.98 ± 0.90	0.94	−5.08	3.86–3.95
$Au_{50}Pd_{50}$	1:30:30	2.92 ± 0.63	0.91	−4.45	3.77–3.92
$Au_{67}Pd_{33}$	1:40:20	3.07 ± 1.22	0.89	−3.52	3.71–3.89
$Au_{80}Pd_{20}$	1:48:12	2.69 ± 0.80	0.88	−3.16	3.73–3.89
Au_{100}	1:60:0	2.66 ± 0.44	0.86	−2.35	3.40–3.76
Pt/C	–	–	0.95	−4.72	3.83–3.94

Representative TEM and HRTEM images of $Au_{33}Pd_{67}$ are shown in Figure 1a and b. The HRTEM images illustrate the fine, crystalline, and continuous well-defined lattice fringes. The *d*-spacing of the adjacent fringes is 0.232 nm, which is quite close to that of AuPd alloy (0.230 nm). Interestingly, the lattice spacing is located between that of pure Au (0.2355 nm, JCPDS-04–0784) and pure Pd (0.2285 nm, JCPDS-01–087–0641), which suggests the formation of AuPd alloy.[45,46] The line-scan profile can be extrapolated from the high-angle annular dark-field (HAADF) scanning transmission electron microscopy (STEM) image (Figure 1c, inset). From the start to the end, Au and Pd possess an almost identical distribution trend. The overlapped feature in the line-scan profile indicates the formation of a AuPd alloyed structure. Moreover, the distribution of the elements was probed by using bright-field transmission electron microscopy (BFTEM; Figure 1d–g). From the energy-dispersive X-ray spectroscopy (EDS) mapping, we can see that both Au and Pd elements were well intermixed, which shows that a peptide-based AuPd alloyed structure was obtained.

The structures of Au_{100}, Pd_{100}, and $Au_{33}Pd_{67}$ were then investigated using XRD. The representative diffraction peaks of $Au_{33}Pd_{67}$ particles are located at $2\theta = 39.1$, 45.1, 66.3, and 79.6, which are assigned to the (111), (200), (220), and (311)

© 2017 Wiley-VCH Verlag GmbH & Co. KGaA, Weinheim

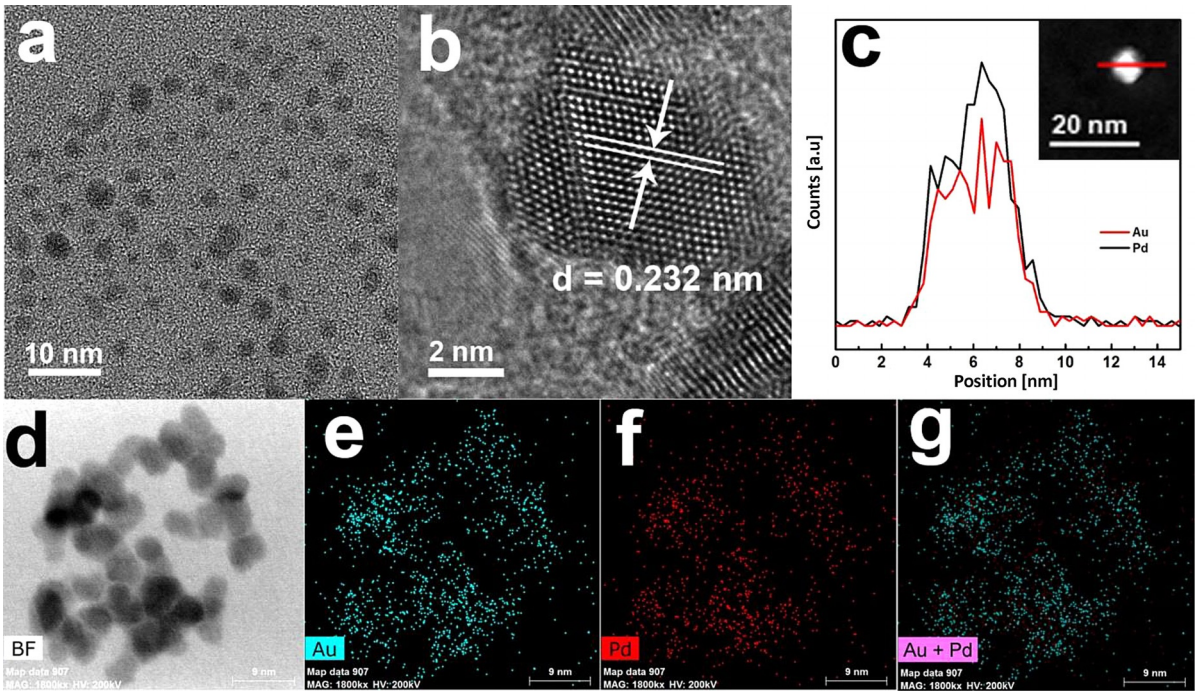

Figure 1. a) Representative TEM image of $Au_{33}Pd_{67}$ NPs, b) HRTEM image and c) HAADF-STEM image and cross-sectional compositional line profiles of a single $Au_{33}Pd_{67}$ NP, d) BFTEM image of the $Au_{33}Pd_{67}$ NPs, and EDS elemental mapping of e) Au, f) Pd, and g) Au+Pd in the NPs. d)–g) Scale bar = 9 nm.

planes of the face-centered cubic alloyed structure (Figure 2a). Furthermore, the diffraction peaks are located between those of pure Au (JCPDS-04–0784) and pure Pd (JCPDS-01-087-0641), which confirms the formation of alloyed AuPd structures.[47,48]

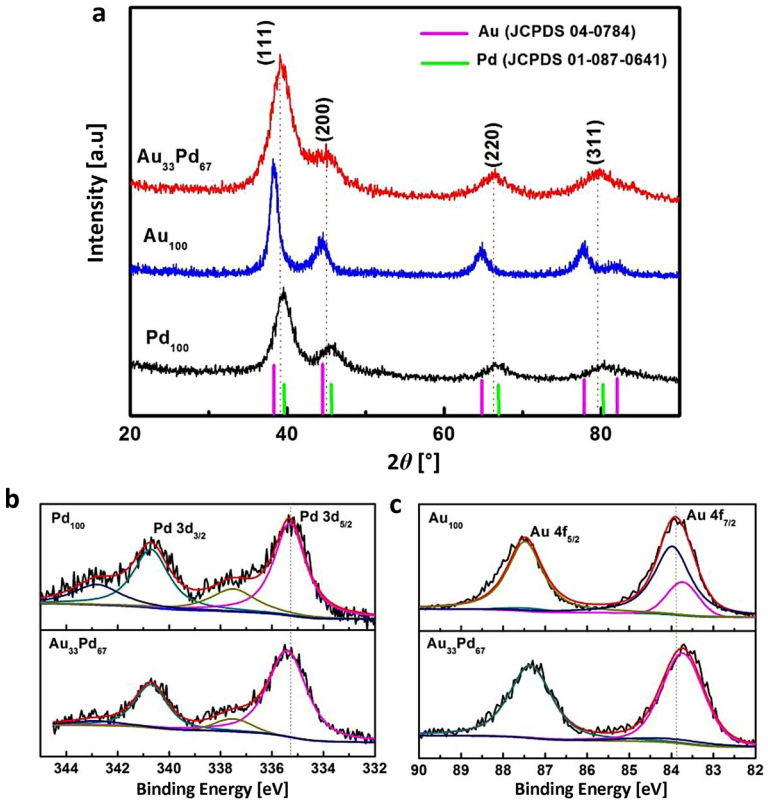

Figure 2. The XRD patterns a) of $Au_{33}Pd_{67}$, Au_{100}, and Pd_{100} and high-resolution XPS spectra of $Au_{33}Pd_{67}$ of b) Pd 3d and c) Au 4f electrons and Pd_{100} or Au_{100} samples.

© 2017 Wiley-VCH Verlag GmbH & Co. KGaA, Weinheim

The chemical composition of the series was analyzed by using X-ray photoelectron spectroscopy (XPS).[49] The survey spectra of Pd_{100}, $Au_{33}Pd_{67}$, and Au_{100} are shown in Figure S3. For $Au_{33}Pd_{67}$, sharp peaks from both the Pd 3d and Au 4f electrons can be identified easily. The high-resolution spectra of the Pd 3d and Au 4f electrons of $Au_{33}Pd_{67}$, Au_{100}, and Pd_{100} are shown in Figure 2b and c. The Pd 3d spectra of $Au_{33}Pd_{67}$ and Pd_{100} can be deconvoluted into two doublets. The pairs at lower binding energies (BE ≈335.2 and 340.7 eV) agree well with metallic Pd,[32,50] whereas the pairs at higher energies (BE ≈337.5 and 342.6 eV) could be ascribed as Pd^{II} species (Figure 2b). This indicates the formation of a substantial amount of palladium oxide. Interestingly, compared with that of Pd_{100}, the Pd $3d_{5/2}$ BE for $Au_{33}Pd_{67}$ shifted positively by approximately 0.2 eV. This can be attributed to electron transfer from Pd to Au as Au is more electronegative than Pd. Strong signals at BE ≈83.5 and 87.3 eV can be ascribed to the Au $4f_{7/2}$ and Au $4f_{5/2}$ electrons (Figure 2c).[51,52] Conversely, compared with Au_{100}, the BE of the Au $4f_{7/2}$ electrons for $Au_{33}Pd_{67}$ decreased by approximately 0.3 eV, which further confirmed the electron transfer from Pd to Au.[32] In addition, the Au/Pd atomic ratios detected by using XPS are given in Table S1, and the values agree well with the initial loading ratios.

The series of samples was next subjected to an electrocatalytic test for the ORR. The ORR activities of our samples and Pt/C are summarized in Table 1. The electrocatalytic activities were first compared by using cyclic voltammetry (CV) and rotating-ring disk electrode (RRDE) voltammetric measurements in oxygen-saturated 0.1 M KOH solution in the potential range of −0.04 to +1.16 V. A sharp cathodic current peak at approximately +0.85 V attributed to oxygen reduction was observed in the CV curves (Figure S4), which indicated all the samples possessed an effective ORR activity. The cathodic peak potentials were estimated as +0.81, +0.80, +0.83, +0.86, +0.86, +0.83, and +0.81 V for Au_{100}, $Au_{80}Pd_{20}$, $Au_{67}Pd_{33}$, $Au_{50}Pd_{50}$, $Au_{33}Pd_{67}$, $Au_{20}Pd_{80}$, and Pd_{100}, respectively. $Au_{50}Pd_{50}$ and $Au_{33}Pd_{67}$ outperformed the other samples in the series.

The ORR activity of these alloyed AuPd NPs was further probed by using a RRDE test. The RRDE voltammograms of the samples at a rotation rate of 1600 rpm are shown in Figure 3.

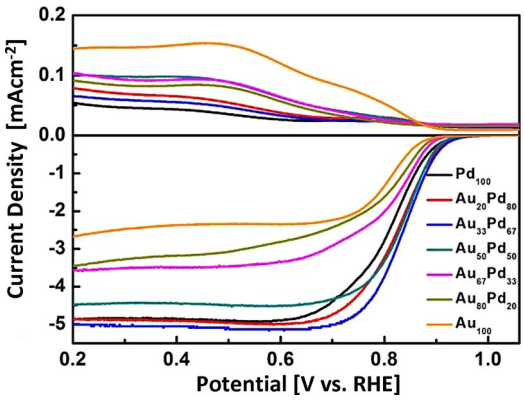

Figure 3. RRDE voltammograms of a glassy carbon electrode of AuPd alloy NPs in O_2-saturated 0.1 M KOH solution. Potential scan rate = 10 mV s^{-1} and the rotation rate = 1600 rpm.

Notably, the onset potential and diffusion-limited current density of the samples varied drastically between samples with different Au/Pd ratios. The onset potential is +0.86, +0.88, +0.89, +0.91, +0.94, +0.90, and +0.89 V for Au_{100}, $Au_{80}Pd_{20}$, $Au_{67}Pd_{33}$, $Au_{50}Pd_{50}$, $Au_{33}Pd_{67}$, $Au_{20}Pd_{80}$, and Pd_{100}, respectively. Moreover, the diffusion-limited current density can be estimated as −2.35, −3.16, −3.52, −4.45, −5.08, −4.91, and −4.83 mA cm^{-2} for Au_{100}, $Au_{80}Pd_{20}$, $Au_{67}Pd_{33}$, $Au_{50}Pd_{50}$, $Au_{33}Pd_{67}$, $Au_{20}Pd_{80}$, and Pd_{100}, respectively. $Au_{33}Pd_{67}$ possesses the most positive onset potential and the largest diffusion-limited current density. The result corresponds well with the above findings and attests that $Au_{33}Pd_{67}$ exhibited the best ORR activity among the series.

As $Au_{33}Pd_{67}$ exhibited the best activity, its ORR performance was further investigated and compared with that of commercial Pt/C. The voltammetric currents increased with the increase of the electrode rotation rate. In N_2-saturated 0.1 M KOH solution, featureless voltammetric currents can be observed for both $Au_{33}Pd_{67}$ and commercial Pt/C. If the solution was switched to O_2-saturated 0.1 M KOH solution, a cathodic peak emerged at approximately 0.88 V for both $Au_{33}Pd_{67}$ and commercial Pt/C, which implies effective catalytic activity (Figure 4b). From the polarization curve presented in Figure 4c, the onset potential was determined as +0.94 V, which approaches that of commercial Pt/C (+0.95 V). However, at 1600 rpm, the diffusion-limited current density of $Au_{33}Pd_{67}$ (5.08 mA cm^{-2}) was much larger than that of commercial Pt/C (4.72 mA cm^{-2}). Overall, the ORR activity of $Au_{33}Pd_{67}$ is at least comparable with, if not better than, commercial Pt/C. The linear sweep voltammetry (LSV) curves of the other samples and Pt/C at different rotation rates are shown in Figures S5 and S6.

Furthermore, from the RRDE voltammetric measurements, the electron transfer number (n) and yield of H_2O_2 can be calculated from Equations (1) and (2), respectively:

$$n = \frac{4I_d}{I_d + I_r/N} \quad (1)$$

$$H_2O_2 = \frac{200I_r/N}{I_r/N + I_d} \quad (2)$$

in which I_d is the disk current, I_r is the ring current, and N is the RRDE collection efficiency (0.37). The n values and H_2O_2 yields of the AuPd alloys and commercial Pt/C are presented in Figure 4d. Within the wide potential range of +0.2 to +0.8 V, the n value of the $Au_{33}Pd_{67}$ sample was 3.86–3.95 (Figure 4d and Table 1), which is slightly larger than that of Pt/C (3.83–3.94). Correspondingly, the H_2O_2 yield for the $Au_{33}Pd_{67}$ sample was approximately 6%, which is a little lower than that of Pt/C (≈8%). Again, these results indicate that $Au_{33}Pd_{67}$ behaves similarly to Pt/C in the complete reduction of oxygen to H_2O. Furthermore, the corresponding Koutecky–Levich (K-L) plots within the potential range of +0.39 to +0.6 V for $Au_{33}Pd_{67}$ and Pt/C are shown in Figure 4e and f. For both $Au_{33}Pd_{67}$ and Pt/C, good linearity was exhibited with a rather consistent slope, which indicates first-order reaction kinetics with respect to the O_2 concentration in the solution. In addition, the K-L plots of the other samples in the series are shown in Figure S7, and

© 2017 Wiley-VCH Verlag GmbH & Co. KGaA, Weinheim

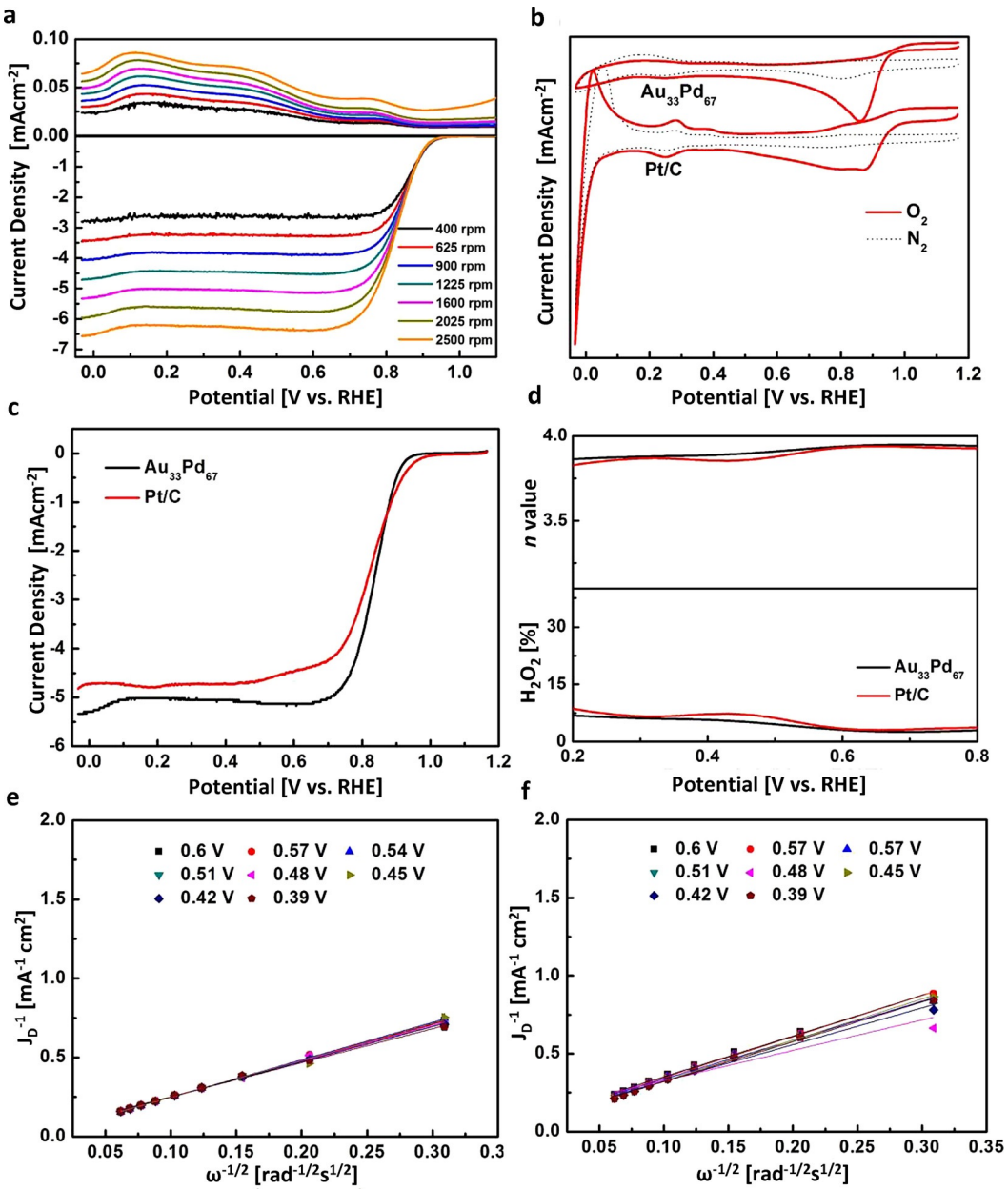

Figure 4. a) LSV curves for $Au_{33}Pd_{67}$ at a rotation rate of 400–2500 rpm. b) CVs, c) RRDE voltammograms, and d) plots of H_2O_2 yield and *n* of a glassy carbon electrode modified with $Au_{33}Pd_{67}$ and Pt/C at a rotation rate of 1600 rpm. The corresponding K-L plots of e) $Au_{33}Pd_{67}$ and f) Pt/C at different electrode potentials. All measurements were performed at a catalyst loading of approximately 81 μg cm^{-2} in an O_2-saturated 0.1 M KOH aqueous solution at a potential scan rate of 10 mV s^{-1}.

almost all the plots demonstrated a good linearity with consistent slopes at different potential values.

The Tafel plots of $Au_{33}Pd_{67}$ and Pt/C are presented in Figure 5, and similar features were observed for $Au_{33}Pd_{67}$ and Pt/C. Two linear regions at low and high overpotentials are present, which has been well documented.[28,53] In the low-overpotential range, the Tafel slope was 50.8 mV dec^{-1} for $Au_{33}Pd_{67}$ and 58.5 mV dec^{-1} for commercial Pt/C. Both of the values are approximately 60 mV dec^{-1}, which implies that the rate-determining step in the ORR process is probably a pseudo-two-electron-transfer reaction.[54–56] However, in the high-overpotential range (above +0.85 V), the slope was 102.3 mV dec^{-1} for $Au_{33}Pd_{67}$ and 115.5 mV dec^{-1} for commercial Pt/C, which indicates that the rate of the reaction was determined by an initial electron transfer to O_2.[57]

Notably, the ORR activity of $Au_{33}Pd_{67}$ is superior to that of the monometallic counterparts, Au_{100} and Pd_{100}. Importantly, with the peptide sequence FlgA3 as the ligand or template, the as-prepared $Au_{33}Pd_{67}$ sample also outperformed AuPd alloys and similar bimetallic structures reported recently. For example, Erikson et al. prepared an electrocatalyst by depositing a Pd coating on Au, and an onset potential of +0.81 V was obtained.[58] The PdAu alloys prepared through the electrodeposition approach by Erikson et al. also showed an onset

© 2017 Wiley-VCH Verlag GmbH & Co. KGaA, Weinheim

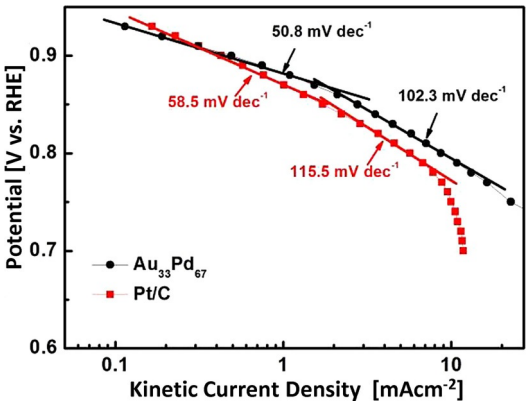

Figure 5. Tafel plots of $Au_{33}Pd_{67}$ and Pt/C obtained from the K-L plot analysis of the RRDE voltammograms (Figures 4e and f).

potential close to +0.81 V. Both of these are much lower than the value of $Au_{33}Pd_{67}$ (+0.94 V).[59] Recently, Feng et al. developed a general strategy for the fabrication of alloyed AuPd flowerlike-assembly nanochains, and the onset potential (+0.94 V) was comparable with that of $Au_{33}Pd_{67}$. However, the half-wave potential (+0.81 V) was much lower than that of $Au_{33}Pd_{67}$ (+0.84 V).[60] This comparison further shows that the peptide-based approach has great potential in the fabrication of bimetallic NPs with enhanced electrocatalytic performances toward the ORR.

Such an excellent ORR performance for $Au_{33}Pd_{67}$ can be accounted for by the Au-alloying Pd-induced electronic effects. Notably, Pd interacts with oxygen strongly (even more strongly than Pt), and Au has very little interaction with oxygen. Compared with Pd alone, the alloying of Au and Pd can diminish the bonding interaction with oxygenated species.[32] Extended X-ray absorption fine structure (EXAFS) studies reported previously revealed that, if the Au content is increased, Pd–O bonding can be suppressed to result in enhanced stability and further formation of a palladium oxide layer.[61] This is caused by the different electronegativity of Au and Pd, as evidenced by the charge transfer behaviors observed by using XPS (Figure 2).

Long-term stability is highly desirable for these bimetallic NPs for catalysis. The durability of $Au_{33}Pd_{67}$ and commercial Pt/C for the ORR were investigated and compared by using chronoamperometry.[38] After continuous operation for approximately 8 h, the cathodic current of $Au_{33}Pd_{67}$ displayed a loss of approximately 7% of the initial value, whereas for commercial Pt/C, the loss was approximately 12% (Figure 6a). This indicates that the long-term stability of $Au_{33}Pd_{67}$ is greater than that of Pt/C under the same conditions. Secondly, the tolerance against methanol crossover is another important

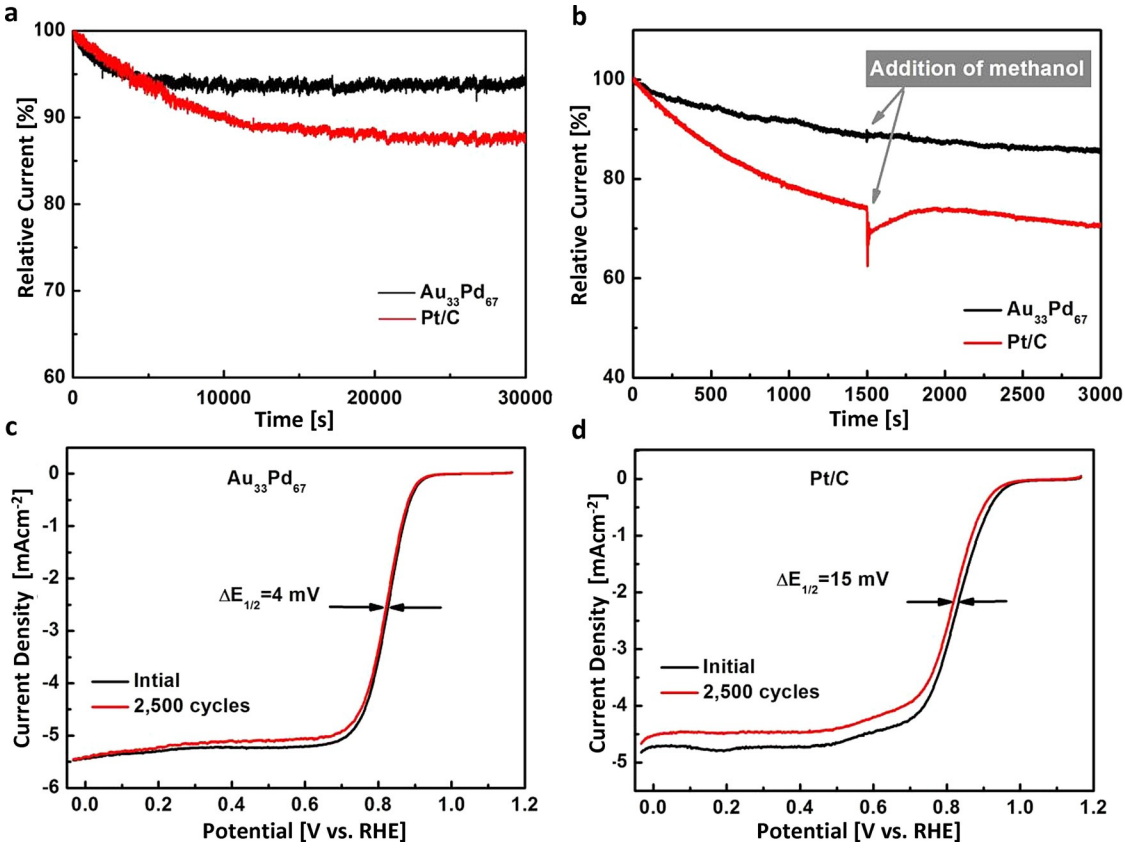

Figure 6. a) Chronoamperometric curves of $Au_{33}Pd_{67}$ and Pt/C at +0.5 V for 30000 s. b) Chronoamperometric curves of $Au_{33}Pd_{67}$ and Pt/C at +0.5 V before and after the addition of methanol (1 M), and c) $Au_{33}Pd_{67}$ and d) Pt/C before and after 2500 cycles of stability testing. All measurements were conducted in an O_2-saturated 0.1 M KOH aqueous solution.

© 2017 Wiley-VCH Verlag GmbH & Co. KGaA, Weinheim

concern to evaluate the durability.[62] For the commercial Pt/C electrode (red curve), the addition of 1 M methanol into the electrolyte solution caused a sudden decrease of the voltammetric current, which can be attributed to methanol oxidation on the surface of the electrode (Figure 6b). Notably, it took approximately 400 s to recover the value to that before the addition of methanol, however, for $Au_{33}Pd_{67}$, little decrease of the current is observed, which suggests a much better methanol tolerance. To assess the stability of the catalyst, accelerated durability tests were conducted by cycling the catalyst over the potential range of +0.6 to +1.0 V at 50 mV s^{-1} in O_2-saturated 0.1 M KOH solution for both $Au_{33}Pd_{67}$ and Pt/C.[31] The half-wave potential of commercial Pt/C shifted negatively by 15 mV after 2500 continuous cycles (Figure 6d), whereas $Au_{33}Pd_{67}$ displayed a much smaller negative shift of only 4 mV (Figure 6c). All these results imply strongly that $Au_{33}Pd_{67}$ possesses a significantly higher long-term stability than Pt/C.

Conclusions

We demonstrate the fabrication of peptide-FlgA3-based AuPd bimetallic nanoparticles (NPs). The as-prepared NPs demonstrated an effective activity for the electroreduction of O_2. Among a series of samples, $Au_{33}Pd_{67}$ exhibited the best activity, evidenced by its positive onset potential and large diffusion-limited current density. Its activity was comparable to that of a state-of-the-art Pt/C catalyst, and its long-term stability was significantly superior to that of Pt/C. Such a remarkable activity and durability was attributed to the alloying of Au and Pd that induced ensemble and electronic effects as charge transfer behavior was observed from Pd to Au by using X-ray photoelectron spectroscopy. Our findings not only highlight the merits of the peptide-enabled approach but also pave the way for the further rational design of peptide-based bimetallic NPs with optimized electrocatalytic properties and enhanced stability.

Experimental Section

Chemicals

The FlgA3 (DYKDDDDKPAYSSGAPPMPPF, >98%) peptide was purchased from Top-Peptide (Shanghai, China). $HAuCl_4 \cdot 3H_2O$ (99%), K_2PdCl_4 (98%), and $NaBH_4$ (98%) were acquired from Aladdin Industrial Corporation (Shanghai, China). All chemicals were used as received without any purification. The water was supplied by using a Barnstead Nanopure water system and had a resistivity of 18.3 MΩ cm^{-1}.

Synthesis of peptide-based AuPd NPs (Au_xPd_y)

The synthesis of Au_xPd_y (in which *x/y* is the Au/Pd molar ratio: 0:100, 20:80, 33:67, 50:50, 67:33, 80:20, and 100:0) alloyed NPs was conducted by following a modification of a procedure reported previously.[21,41] For the synthesis of $Au_{33}Pd_{67}$, $HAuCl_4$ (33 μL, 0.02 M), K_2PdCl_4 (67 μL, 0.02 M), FlgA3 solution (77 μL, 1 mg mL^{-1}), and H_2O (1723 μL) were first mixed and stirred for 15 min, then freshly prepared $NaBH_4$ (100 μL, 0.1 M) aqueous solution was added dropwise under shaking. The solution turned from pale yellow into a charcoal color immediately and it was left undisturbed for 1 h. The peptide-based AuPd alloyed NPs were obtained. Pd_{100}, $Au_{20}Pd_{80}$, $Au_{50}Pd_{50}$, $Au_{67}Pd_{33}$, $Au_{80}Pd_{20}$, and Au_{100} were synthesized in a similar manner in which the FlgA3 concentration was kept constant and the metal concentration was changed correspondingly.

Characterization and electrochemical measurements

UV/Vis absorbance spectra were acquired by using a Shimadzu 2600/2700 UV/Vis scanning spectrophotometer with a 1 cm quartz cuvette. The microscopic images were obtained by using a JEM-2100F coupled with HAADF-STEM imaging at an acceleration voltage of 200 kV. Further surface structure was observed by using FEI Titan Themis 200 HRTEM, and BF-TEM images and elemental mapping were recorded by using a Bruker super-X energy dispersive spectrometer. XPS was performed by using an Escalab 250 photoelectron spectrometer (Thermo fisher scientific, USA). Electrochemical measurements were conducted by using a CHI 750E electrochemical workstation (CH Instruments Inc.) in a 0.1 M KOH aqueous solution at RT. A Pt wire and a Ag/AgCl electrode ($E_{Ag/AgCl} = E_{RHE} + 0.966$ V, RHE = reversible hydrogen electrode) were used as the counter electrode and reference electrode, respectively. The working electrode was a ring disk electrode (diameter 5.61 mm) with a geometrical area of 0.2475 cm^2, which was cleaned by mechanical polishing with aqueous slurries of 0.3 μm alumina powders on a polishing microcloth. The catalyst loading was approximately 81 μg cm^{-2} for all the samples. For Pd_{100}, 36.1 μL of the catalyst ink was cast dropwise onto the glassy carbon disk and dried at RT, and the corresponding addition volumes of $Au_{20}Pd_{80}$, $Au_{33}Pd_{67}$, $Au_{50}Pd_{50}$, $Au_{67}Pd_{33}$, $Au_{80}Pd_{20}$, and Au_{100} were 35.9, 35.8, 35.7, 35.5, 35.4, and 35.3 μL respectively. For Pt/C (20 wt%), Pt/C (2 mg) was added to ethanol (1 mL), and 10 μL of the dispersion was cast dropwise onto the glassy carbon disk electrode and dried at RT. The Ag/AgCl reference electrode was calibrated with respect to a RHE. The calibration was conducted in a high-purity H_2 (99.999%) saturated electrolyte with a Pt wire as both the working electrode and counter electrode. Cyclic voltammograms were acquired at a scan rate of 10 mV s^{-1} in 0.1 M KOH solution, and the average of the two potentials at which the current crossed zero was taken as the thermodynamic potential of the RHE. A gold ring electrode was employed in the LSV measurements, and the measurements were conducted in an O_2-saturated 0.1 M KOH solution at different rotation rates (100–2500 rpm) in the potential range of −0.04 to 1.16 V. For detection of peroxide, the ring electrode potential was set at +0.5 V (vs. Ag/AgCl) at which H_2O_2 can be oxidized completely into water. The RRDE voltammetric measurements were conducted in the potential range of −0.04 V to +1.16 V at a rotation rate of 1600 rpm, and the ring potential was set at +0.5 V. Chronoamperometric responses and methanol crossover measurements were conducted in an O_2-saturated 0.1 M KOH solution at +0.5 V for 30000 s, and accelerated durability tests (ADT) were performed by cycling the catalyst over the potential range of +0.6 V to +1.0 V at 50 mV s^{-1} in O_2-saturated 0.1 M KOH solution.

Acknowledgements

We acknowledge financial support from the National Natural Science Foundation of China (No. 21501059 for Z.H.T. and No. 21373061 for X.F.W.), Project of Public Interest Research and Capacity Building of Guangdong Province (2015A010105009),

© 2017 Wiley-VCH Verlag GmbH & Co. KGaA, Weinheim

Guangdong Natural Science Funds for Distinguished Young Scholars (No. 2015A030306006), and Guangdong Innovative and Entrepreneurial Research Team Program (No. 2014ZT05N200).

Conflict of interest

The authors declare no conflict of interest.

Keywords: alloys · gold · palladium · peptides · reduction

[1] K. D. Gilroy, A. Ruditskiy, H.-C. Peng, D. Qin, Y. Xia, *Chem. Rev.* **2016**, *116*, 10414 – 10472.
[2] F. Tao, *Chem. Soc. Rev.* **2012**, *41*, 7977 – 7979.
[3] M. Sankar, N. Dimitratos, P. J. Miedziak, P. P. Wells, C. J. Kiely, G. J. Hutchings, *Chem. Soc. Rev.* **2012**, *41*, 8099 – 8139.
[4] E. Roduner, *Chem. Soc. Rev.* **2006**, *35*, 583 – 592.
[5] W. Chen, J. Kim, S. Sun, S. Chen, *Langmuir* **2007**, *23*, 11303 – 11310.
[6] N. Toshima, T. Yonezawa, *New J. Chem.* **1998**, *22*, 1179 – 1201.
[7] H. Qian, D.-e. Jiang, G. Li, C. Gayathri, A. Das, R. R. Gil, R. Jin, *J. Am. Chem. Soc.* **2012**, *134*, 16159 – 16162.
[8] H. Qian, E. Barry, Y. Zhu, R. Jin, *Acta Phys.-Chim. Sin.* **2011**, *27*, 513 – 519.
[9] I. N. Francesco, F. Fontaine-Vive, S. Antoniotti, *ChemCatChem* **2014**, *6*, 2784 – 2791.
[10] J. Fabrega, S. R. Fawcett, J. C. Renshaw, J. R. Lead, *Environ. Sci. Technol.* **2009**, *43*, 7285 – 7290.
[11] I. Willner, R. Baron, B. Willner, *Adv. Mater.* **2006**, *18*, 1109 – 1120.
[12] N. S. R. Satyavolu, L. H. Tan, Y. Lu, *J. Am. Chem. Soc.* **2016**, *138*, 16542 – 16548.
[13] K. N. L. Huggins, A. P. Schoen, M. A. Arunagirinathan, S. C. Heilshorn, *Adv. Funct. Mater.* **2014**, *24*, 7737 – 7744.
[14] C.-L. Chen, N. L. Rosi, *Angew. Chem. Int. Ed.* **2010**, *49*, 1924 – 1942; *Angew. Chem.* **2010**, *122*, 1968 – 1986.
[15] M. B. Dickerson, K. H. Sandhage, R. R. Naik, *Chem. Rev.* **2008**, *108*, 4935 – 4978.
[16] R. Bhandari, R. Coppage, M. R. Knecht, *Catal. Sci. Technol.* **2012**, *2*, 256 – 266.
[17] B. D. Briggs, M. R. Knecht, *J. Phys. Chem. Lett.* **2012**, *3*, 405 – 418.
[18] N. A. Merrill, E. M. McKee, K. C. Merino, L. F. Drummy, S. Lee, B. Reinhart, Y. Ren, A. I. Frenkel, R. R. Naik, N. M. Bedford, M. R. Knecht, *ACS Nano* **2015**, *9*, 11968 – 11979.
[19] Y.-S. Ko, Y.-T. Kim, J.-H. Kim, D. H. Kim, K.-H. Kim, W. S. Yun, Y. D. Kim, J. Lee, Y. H. Kim, *CrystEngComm* **2016**, *18*, 6024 – 6028.
[20] N. M. Bedford, A. R. Showalter, T. J. Woehl, Z. E. Hughes, S. Lee, B. Reinhart, S. P. Ertem, E. B. Coughlin, Y. Ren, T. R. Walsh, B. A. Bunker, *ACS Nano* **2016**, *10*, 8645 – 8659.
[21] Q. Wang, Z. Tang, L. Wang, H. Yang, W. Yan, S. Chen, *ChemistrySelect* **2016**, *1*, 6044 – 6052.
[22] H. Yang, Z. Tang, W. Yan, L. Wang, Q. Wang, Y. Zhang, Z. Liu, S. Chen, *J. Alloys Compd.* **2017**, *702*, 146 – 152.
[23] M. K. Debe, *Nature* **2012**, *486*, 43 – 51.
[24] M. Winter, R. J. Brodd, *Chem. Rev.* **2004**, *104*, 4245 – 4270.
[25] A. Kraytsberg, Y. Ein-Eli, *Energy Fuels* **2014**, *28*, 7303 – 7330.
[26] M. Liu, R. Zhang, W. Chen, *Chem. Rev.* **2014**, *114*, 5117 – 5160.
[27] J. Yin, Y. Li, F. Lv, Q. Fan, Y.-Q. Zhao, Q. Zhang, W. Wang, F. Cheng, P. Xi, S. Guo, *ACS Nano* **2017**, *11*, 2275 – 2283.
[28] S. Guo, S. Zhang, S. Sun, *Angew. Chem. Int. Ed.* **2013**, *52*, 8526 – 8544; *Angew. Chem.* **2013**, *125*, 8686 – 8705.
[29] L. Bu, N. Zhang, S. Guo, X. Zhang, J. Li, J. Yao, T. Wu, G. Lu, J.-Y. Ma, D. Su, X. Huang, *Science* **2016**, *354*, 1410 – 1414.
[30] M. Li, Z. Zhao, T. Cheng, A. Fortunelli, C.-Y. Chen, R. Yu, Q. Zhang, L. Gu, B. V. Merinov, Z. Lin, E. Zhu, T. Yu, Q. Jia, J. Guo, L. Zhang, W. A. Goddard, Y. Huang, X. Duan, *Science* **2016**, *354*, 1414 – 1419.
[31] L. Wang, Z. Tang, W. Yan, Q. Wang, H. Yang, S. Chen, *J. Power Sources* **2017**, *343*, 458 – 466.
[32] C. P. Deming, A. Zhao, Y. Song, K. Liu, M. M. Khan, V. M. Yates, S. Chen, *ChemElectroChem* **2015**, *2*, 1719 – 1727.
[33] L. Wang, Z. Tang, X. Liu, W. Niu, K. Zhou, H. Yang, W. Zhou, L. Li, S. Chen, *RSC Adv.* **2015**, *5*, 103421 – 103427.
[34] Q. Wang, L. Wang, Z. Tang, F. Wang, W. Yan, H. Yang, W. Zhou, L. Li, X. Kang, S. Chen, *Nanoscale* **2016**, *8*, 6629 – 6635.
[35] C. P. Deming, R. Mercado, V. Gadiraju, S. W. Sweeney, M. Khan, S. Chen, *ACS Sustainable Chem. Eng.* **2015**, *3*, 3315 – 3323.
[36] C. P. Deming, R. Mercado, J. E. Lu, V. Gadiraju, M. Khan, S. Chen, *ACS Sustainable Chem. Eng.* **2016**, *4*, 6580 – 6589.
[37] L.-L. He, P. Song, J.-J. Feng, W.-H. Huang, Q.-L. Wang, A.-J. Wang, *Electrochim. Acta* **2015**, *176*, 86 – 95.
[38] W. Yan, Z. Tang, L. Wang, Q. Wang, H. Yang, S. Chen, *Int. J. Hydrogen Energy* **2017**, *42*, 218 – 227.
[39] J. M. Slocik, R. R. Naik, *Adv. Mater.* **2006**, *18*, 1988 – 1992.
[40] J. M. Slocik, M. O. Stone, R. R. Naik, *Small* **2005**, *1*, 1048 – 1052.
[41] H. Yang, Z. Tang, L. Wang, W. Zhou, L. Li, Y. Zhang, S. Chen, *Mater. Sci. Eng. B* **2016**, *210*, 37 – 42.
[42] R. W. Murray, *Chem. Rev.* **2008**, *108*, 2688 – 2720.
[43] R. Jin, C. Zeng, M. Zhou, Y. Chen, *Chem. Rev.* **2016**, *116*, 10346 – 10413.
[44] S. Chen, A. C. Templeton, R. W. Murray, *Langmuir* **2000**, *16*, 3543 – 3548.
[45] J. W. Hong, Y. W. Lee, M. Kim, S. W. Kang, S. W. Han, *Chem. Commun.* **2011**, *47*, 2553 – 2555.
[46] J.-N. Zheng, S.-S. Li, X. Ma, F.-Y. Chen, A.-J. Wang, J.-R. Chen, J.-J. Feng, *J. Power Sources* **2014**, *262*, 270 – 278.
[47] L. Shi, A. Wang, T. Zhang, B. Zhang, D. Su, H. Li, Y. Song, *J. Phys. Chem. C* **2013**, *117*, 12526 – 12536.
[48] J.-J. Lv, S.-S. Li, A.-J. Wang, L.-P. Mei, J.-R. Chen, J.-J. Feng, *Electrochim. Acta* **2014**, *136*, 521 – 528.
[49] H. Gu, C. Ma, J. Gu, J. Guo, X. Yan, J. Huang, Q. Zhang, Z. Guo, *J. Mater. Chem. C* **2016**, *4*, 5890 – 5906.
[50] J. F. Moulder, W. F. Stickle, P. E. Sobol, K. D. Bomben, *Handbooks of X-ray Photoelectron Spectroscopy*, PerkinElmer, Minnesota, USA, **1992**.
[51] Z. Tang, D. A. Robinson, N. Bokossa, B. Xu, S. Wang, G. Wang, *J. Am. Chem. Soc.* **2011**, *133*, 16037 – 16044.
[52] P. Zhang, *J. Phys. Chem. C* **2014**, *118*, 25291 – 25299.
[53] C.-H. Cui, S.-H. Yu, *Acc. Chem. Res.* **2013**, *46*, 1427 – 1437.
[54] G. He, Y. Song, K. Liu, A. Walter, S. Chen, S. Chen, *ACS Catal.* **2013**, *3*, 831 – 838.
[55] C. Lin, Y. Song, L. Cao, S. Chen, *ACS Appl. Mater. Interfaces* **2013**, *5*, 13305 – 13311.
[56] Y. Liang, Y. Li, H. Wang, J. Zhou, J. Wang, T. Regier, H. Dai, *Nat. Mater.* **2011**, *10*, 780 – 786.
[57] L. Wang, Z. Tang, W. Yan, H. Yang, Q. Wang, S. Chen, *ACS Appl. Mater. Interfaces* **2016**, *8*, 20635 – 20641.
[58] H. Erikson, M. Liik, A. Sarapuu, M. Marandi, V. Sammelselg, K. Tammeveski, *J. Electroanal. Chem.* **2013**, *691*, 35 – 41.
[59] H. Erikson, A. Sarapuu, J. Kozlova, L. Matisen, V. Sammelselg, K. Tammeveski, *Electrocatalysis* **2015**, *6*, 77 – 85.
[60] L.-L. He, P. Song, A.-J. Wang, J.-N. Zheng, L.-P. Mei, J.-J. Feng, *J. Mater. Chem. A* **2015**, *3*, 5352 – 5359.
[61] C. Koenigsmann, E. Sutter, R. R. Adzic, S. S. Wong, *J. Phys. Chem. C* **2012**, *116*, 15297 – 15306.
[62] J. Liu, L. Li, W. Niu, N. Wang, D. Zhao, S. Zeng, S. Chen, *ChemElectroChem* **2016**, *3*, 1116 – 1123.

Manuscript received: February 14, 2017
Revised manuscript received: March 22, 2017
Accepted manuscript online: March 23, 2017
Version of record online: June 12, 2017

© 2017 Wiley-VCH Verlag GmbH & Co. KGaA, Weinheim